solids

MDPI

Article

Direct Synthesis of CuP_2 and Cu_3P and Their Performance as Electrocatalysts for Hydrogen Evolution, Oxygen Evolution, and Oxygen Reduction Reactions

Xiao Ma [1,2,3], Xueni Huang [4] and Abdessadek Lachgar [1,2,3,*]

[1] Department of Chemistry, Wake Forest University, Winston-Salem, NC 27109, USA; max217@wfu.edu
[2] Center for Energy, Environment and Sustainability (CEES), Wake Forest University, Winston-Salem, NC 27109, USA
[3] Center for Functional Materials (CFM), Wake Forest University, Winston-Salem, NC 27109, USA
[4] Department of Chemistry, University of Connecticut, Storrs, CT 06269, USA; xueni.huang@uconn.edu
* Correspondence: lachgar@wfu.edu; Tel.: +1-(336)-758-4676

Abstract: Copper phosphides are promising materials for energy conversion applications because of their unique electronic structure and controllable composition. Two stoichiometric copper phosphides, CuP_2 and Cu_3P, were prepared by direct wet-chemical synthesis using red phosphorus. They were characterized by powder X-ray diffraction, scanning and transmission electron microscopy, and X-ray photoelectron spectroscopy. The precursor selection, reaction temperature, time and solvent composition were also studied. CuP_2 is the thermodynamically more stable product, but Cu_3P is more commonly obtained. This work demonstrated that higher temperature helps in CuP_2 formation. More importantly, using more trioctylphosphine oxide helps control the morphology leading to crystal growth along the crystallographic a-axis. CuP_2 and Cu_3P were tested for hydrogen evolution, oxygen evolution, and oxygen reduction reactions. CuP_2 works better for HER in acidic conditions and OER in general, and Cu_3P showed better activity than CuP_2 for HER and ORR in an alkaline medium. This study has led to a simple approach to the synthesis of CuP_2 nanowires.

Keywords: transition metal phosphide; copper phosphide; electrocatalysis

Citation: Ma, X.; Huang, X.; Lachgar, A. Direct Synthesis of CuP_2 and Cu_3P and Their Performance as Electrocatalysts for Hydrogen Evolution, Oxygen Evolution, and Oxygen Reduction Reactions. *Solids* **2024**, *5*, 140–150. https://doi.org/10.3390/solids5010010

Academic Editors: Manickam Minakshi and Stefano Agnoli

Received: 18 October 2023
Revised: 19 February 2024
Accepted: 23 February 2024
Published: 7 March 2024

1. Introduction

Electrocatalytic energy conversion offers an efficient and environmentally friendly route for the conversion and storage of electrical energy. Significant advances have been achieved in understanding the intricacies of essential electrocatalytic reactions. Groundbreaking advancements have been achieved in understanding hydrogen evolution (HER), oxygen evolution (OER), and oxygen reduction (ORR) [1,2]. Electrocatalysts such as platinum-based materials [3,4] are well-known for their exceptional performance in terms of efficiency and durability for both water electrolysis and fuel cells, but it is highly desirable yet challenging to develop efficient non-platinum group metal (non-PGM) electrocatalysts [5,6]. Compared with PGM catalysts, non-PGM catalysts usually suffer from low efficiency and poor durability, but some transition metal-based materials such as transition metal phosphides have demonstrated potential as electrocatalysts, for the hydrogen evolution reaction (HER) [7,8]. Likewise, Ni-Fe-layered double hydroxides have been shown to act as good electrocatalysts for the oxygen evolution reaction (OER) [9], and iron-nitrogen-carbon active structures have been studied as electrocatalysts for oxygen reduction (ORR) [10,11]. Unlike Fe-based materials, Cu-based materials have been less studied, despite the fact that they have shown potential as an oxygen evolution catalyst [12]. In fact, some homogeneous ORR catalysts with copper (enzyme laccase [13,14] for instance) have been reported to have the highest onset potential, which suggest their potential as efficient electrocatalysts. Thus, Cu-based materials can be important in developing non-PGM electrocatalysts in energy conversion and other applications.

Phosphides have been reported as robust HER and ORR catalysts, and incorporating phosphorus can increase the catalyst robustness compared to metal alone [15,16]. To study the role of phosphorus in electrochemical reactions and gain a better understanding of the structure–performance relationship, it is important to study different forms of copper. CuP_2 and Cu_3P are the most common stoichiometric copper phosphides. CuP_2 is considered to be the more thermodynamically stable binary, but has been less studied than Cu_3P [17]. It crystallizes in the monoclinic space group $P2_1/c$, where Cu(I) is coordinated by four P atoms forming a distorted tetrahedral [18]. In terms of valency, half of the P atoms are formally neutral, and half can be assigned the oxidation state −1 [19]. Although CuP_2 is the more thermodynamically stable phase [17], common wet-chemical synthesis (with phosphine) always generates Cu_3P [20]. CuP_2 can be synthesized by ball-milling [21,22], solvothermal [23], and solid–gas reaction [24], which usually requires high temperature or vacuum annealing. Barry et al. reported that the synthesis of amorphous CuP_2 by mixing copper chloride and white and red phosphorus as a solid pallet can lower the annealing temperature to 500 °C [25]. This can also be achieved with tin flux at similar temperature [26]. Wolff et al. also used red phosphorus to synthesize copper-deficient Cu_3P in ionic liquids [27].

In this work, direct synthesis of CuP_2 and Cu_3P was achieved by mixing Cu salt and red phosphorous in a mixture of trioctylphosphine oxide (TOPO) and 1-octadecene (ODE) directly at relatively low temperatures without further heat treatment. The use of inexpensive and stable red phosphorus as a reactant for the synthesis of Cu phosphides at lower temperatures by wet synthesis is not only a simple process but is also beneficial for mass production. By using high boiling point solvents, such as TOPO (408 °C) and ODE (317 °C), $CuCl_2$ and red phosphorus resulted in well-crystallized CuP_2 without further annealing. Excess TOPO seems to help in morphology control, leading to the formation of nanowires with a diameter of ~43 nm. In this paper, the direct synthesis of Cu_3P and CuP_2 and how the different phosphorus content affects their electrochemical performance is investigated.

2. Materials and Methods

2.1. Chemicals

Amorphous red phosphorus (−100 mesh, Alfa Aesar, Ward Hill, MA, USA, 98.9%), trioctylphosphine oxide (TOPO, STREM Chemicals, Newburyport, MA, USA, 99%), anhydrous copper (II) chloride (STREM Chemicals, Newburyport, MA, USA, min 98%), and 1-Octadecene (ODE, Aldrich, St. Louis, MO, USA, 90%) were used without further purification.

The crystal structure data of Cu_3P and CuP_2 were summarized in Table 1.

Table 1. Crystal structures for Cu_3P and CuP_2.

Chemical Composition	**Cu_3P ***	**CuP_2**
Space Group	$P\bar{3}c1$	$P2_1/c$
Unit cell	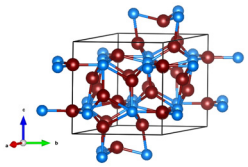	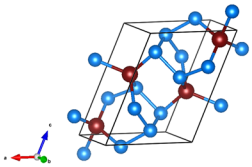
a b c	a = 6.91 Å b = 6.91 Å c = 7.13 Å	a = 5.77 Å b =4.78 Å c = 7.50 Å
α β γ	α = 90.00° β = 90.00° γ = 120.00°	α = 90° β = 112.63° γ = 90.00°

Table 1. *Cont.*

Chemical Composition	Cu_3P *	CuP_2
# JCPDS	02-1263	18-0452
ICSD code	26775	35282
# Materials Project	mp-14012	mp-927

* There are other phases for Cu_3P, including $P\bar{3}P\bar{3}m1$ and P63cm. The latter one has similar symmetry and unit cell, making it hard to differentiate with $P\bar{3}c1$. All the analysis was based on $P\bar{3}c1$ in this paper.

2.2. Synthesis of CuP_2

In a 3-neck round bottom flask, 50 mg (0.37 mmol) of $CuCl_2$, 30 mg (0.96 mmol) of red phosphorus, 8 mL of solvents, and a stir bar were added before connecting the flask to a Schlenk line. The set-up was degassed at 120 °C and purged with nitrogen. The temperature was increased to 320 °C and maintained for 48 h.

2.3. Synthesis of Cu_3P

The setup for the synthesis of Cu_3P was similar to that of CuP_2, with 133 mg (0.99 mmol) of $CuCl_2$, 30 mg (0.96 mmol) of red phosphorus, and 8 mL of solvents. The mixture was degassed, refilled with nitrogen, and refluxed at 250 °C for 48 h.

The as-synthesized samples were washed 3 times with hexane and acetone and redispersed in hexane for future use.

The proposed reactions can be represented by the following chemical equations:

$$3\ CuCl_2 + 8\ P_{red} \rightarrow 3\ CuP_2 + 2\ PCl_3$$
(Reflux at 320 °C, 48 h)

$$3\ CuCl_2 + 3\ P_{red} \rightarrow Cu_3P + 2\ PCl_3$$
(Reflux at 250 °C, 48 h)

2.4. Characterization

Powder X-ray diffraction (PXRD) patterns were collected using a Bruker D2 Phaser (Bruker, Billerica, MA, USA) with 30 kV/10 mA Cu Kα X-ray radiation (1.5406 Å). Scanning electron microscopy (SEM) images were taken on a Zeiss Gemini 300 (Carl Zeiss, Oberkochen, Germany) and the energy dispersive spectroscopy analysis was performed using Bruker XFlash 6-30 (Bruker, Billerica, MA, USA) at 15 kV acceleration voltage. Transmission electron microscopy (TEM) images were acquired with the Thermo Fisher Talos F200i S/TEM (Thermo Fisher Scientific, Waltham, MA, USA) and Ceta camera. X-ray Photoelectron Spectroscopy (XPS) was performed using Thermo Scientific ESCALAB™ Xi+ (Thermo Fisher Scientific, Waltham, MA, USA). The samples were prepared by drop-casting the washed CuP_2 and Cu_3P onto a Si wafer and ion etching for 90 s.

2.5. Electrochemical Performance Study

Electrochemical measurements were acquired using a Gamry electrochemical workstation in a three-electrode system with 0.1 M NaOH as the electrolyte. In a typical experiment, the nanocrystals of CuP_2 and Cu_3P were drop-cast onto glassy carbon (for HER) or carbon cloth (for OER). Specifically, ~10 mg of catalyst was mixed with 10 mg of Vulcan black, dispersed in a mixture of isopropanol and water, and sonicated for 1 h. For the catalyst loading, 10 μL of the catalyst inks were drop-casted on the substrate. The reference electrode used was Ag/AgCl in saturated KCl solution and the counter electrode was a graphite rod. Oxygen reduction reaction measurements were performed on a rotating disk electrode, and 1600 rpm rotating rates were performed to achieve a well-defined oxygen transport condition.

3. Results

3.1. Material Synthesis and Characterization

Common solvents including hexadecane, 1-octadecene (ODE), and trioctylphosphine oxide (TOPO) were tested for the synthesis. Increasing the reaction's temperature will increase the crystallinity of CuP_2. TOPO has the highest boiling point and provides the best results in terms of the crystallinity and morphology control for CuP_2 synthesis at a reaction temperature of 320 °C. Thermodynamic parameter is the predominant factor in synthesis; by altering the reaction temperature with the same recipe, Cu_3P can also be obtained. For the solvents, 10% TOPO and 90% ODE (0.7 g TOPO and 7.2 mL ODE) were used and run at 320, 280, and 250 °C for 48 h (Figure 1a). PXRD data indicate that Cu_3P was the dominant phase at 250 °C, and a mixture of Cu_3P and CuP_2 was obtained at 280 °C. The broad peak in Cu_3P was possibly due to the lower crystallinity at lower reaction temperatures. Despite CuP_2 being the thermodynamically favored product [17], Cu_3P is often favored with common phosphorous precursors such as tris(trimethylsilyl)phosphine or trioctylphosphine in wet-chemical synthesis [20,28]. Therefore, Cu_3P can be obtained at lower reaction temperatures possibly due to a lower energy barrier needed for its formation.

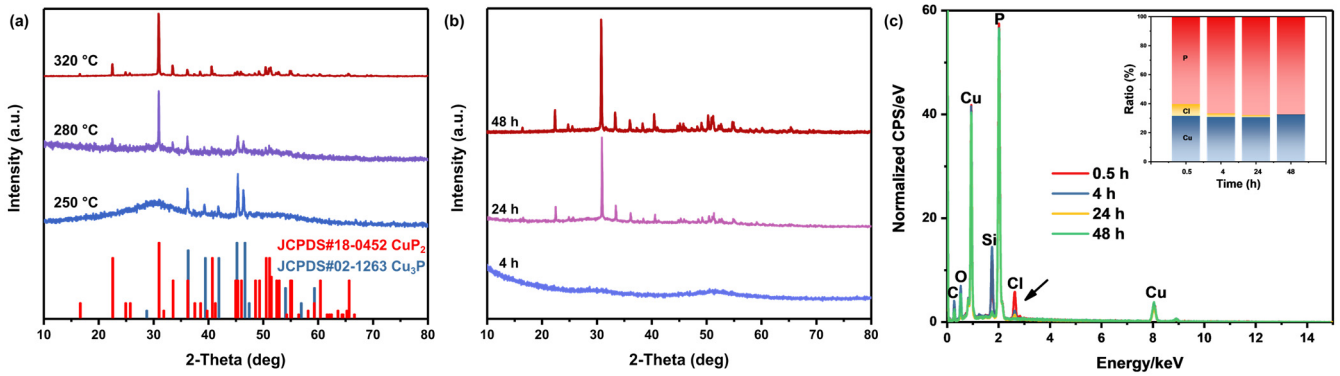

Figure 1. Powder X-ray diffraction patterns of the products were obtained by varying the (**a**) reflux temperature and (**b**) time. (**c**) Normalized energy dispersive spectrum and elemental ratio of Cu:Cl:P (as inset) at different times during CuP_2 synthesis.

PXRD patterns of washed aliquots for CuP_2 synthesis that were run at 320 °C showed the transition from amorphous to crystalline over time, suggesting there is no Cu_3P intermediate for CuP_2 synthesis. Mixing Cu or Cu_3P nanocrystals with red P under similar conditions did not produce CuP_2 either. The time evolution suggests a slow reaction process because of the solid–solid diffusions, and that better crystallinity can be obtained after 24 h. EDS was taken and normalized using the Cu peaks (Figure 1c). The Cl ratio consistently decreases over the reaction time, suggesting the reaction is driven by the removal of PCl_3 species, which is consistent with the literature [25,29].

Besides the effects of different solvents and solvent mixtures, other copper salts were studied (Figure 2). By comparing the relative intensities at 45 degrees (where Cu_3P has the strongest peaks), a higher temperature and a larger TOPO/ODE ratio can help in forming CuP_2. Cu precursors, such as CuCl, copper acetylacetonate ($Cu(acac)_2$), $Cu(NO_3)_2{\cdot}2.5H_2O$, and $CuSO_4{\cdot}5H_2O$ were also tested, and all reactions resulted in the predominant formation of CuP_2. Cu (II) chloride and nitrate worked the best, but the coordination precursor $Cu(acac)_2$, results in more Cu_3P. Commonly used ligands such as oleic acid and oleylamine did not assist in the phosphidation nor the shape control; instead, they hindered the phosphidation process as more Cu_3P products were observed in PXRD. Furthermore, the hot injection did not help in the CuP_2 formation or the shape control. Therefore, although this wet-chemical approach lowered the reaction temperature required for CuP_2 synthesis compared with vacuum annealing, the reaction itself is still similar to a solid-state reaction. TOPO helps the reaction process and temperature is the dominant factor for the conversion.

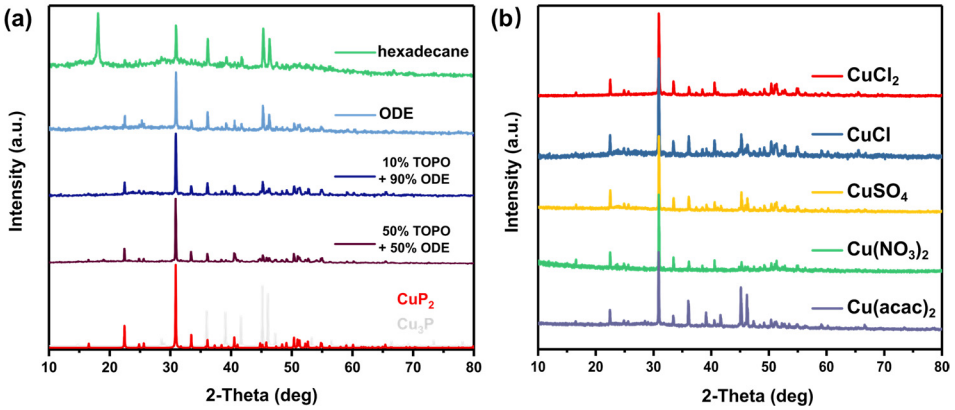

Figure 2. Powder X-ray diffraction results for CuP_2 synthesis by varying the (**a**) temperature and solvents (hexadecane at 280 °C, ODE, 10% TOPO + 90% ODE, and 50% TOPO + 50% ODE at 320 °C) and (**b**) Cu precursor. The reference patterns of Cu_3P and CuP_2 correspond to JCPDS 02-1263 and 18-0452, respectively.

A larger TOPO/ODE ratio not only provides better crystallinity, but also tends to result in wire-shaped structures as shown in the electron microscopy images shown above. For Cu_3P, the morphology is quite random, where small particles aggregate to form large particles. For CuP_2, a larger TOPO/ODE ratio showed a strong tendency to form wire morphology. This might be due to TOPO binding to (0 1 2) crystal faces, allowing the nanocrystals to grow along the crystallographic a-axis, resulting in the observed wire-like shape [30]. The diameter of CuP_2 wires ranges from 25 to 70 nm with the average diameter being 43 nm (Figure S1).

Due to the lower reaction temperature, Cu_3P is formed and less crystallized than CuP_2, and this observation is also consistent with the PXRD results. In the TEM images, 0.20 nm d-spacing can be measured for Cu_3P particles (Figure 3a), which corresponds to (3 0 0) for Cu_3P. In Figure 3b, 0.26 nm lattice spacing can be identified for CuP_2 wires and corresponds to the (2 0 0) plane. For STEM elemental mapping, Cu_3P and CuP_2 both show a homogeneous distribution of Cu and P elements. There is an amorphous shell over CuP_2 as observed in HRTEM and STEM, which is probably due a to solid-state reaction-like mechanism as reported before [31].

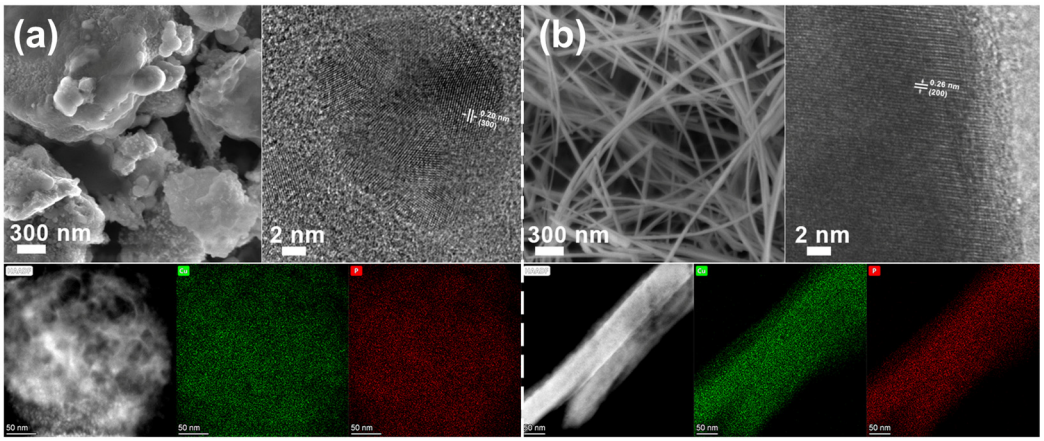

Figure 3. SEM, HR-TEM, and STEM elemental mapping for (**a**) Cu_3P and (**b**) CuP_2.

To further characterize the phases formed, electron diffraction studies were conducted for both Cu_3P and CuP_2 samples. Fourier transform was performed with the squared regions and CrysTBox [32] was used to verify the miller indices and zone axis. For Cu_3P (Figure 4a), the diffraction spots were diffused due to small crystallite sizes and random orientations, but consistent with [001] as the zone axis in general. Two neighboring spots on the edge of a hexagon shape can be indexed as (3 0 0) and (3 −3 0), consistent with the hexagonal lattice symmetry of Cu_3P. For CuP_2 (Figure 4b), the blue and red diffraction spots can be attributed to (2 0 0) and (0 1 2) with a zone axis of [0 −2 1], and a calculated interplane angle of 77.83°, both matching the values measured from the electron diffraction pattern. This also confirms that the growth direction is along the crystallographic a-axis (or [1 0 0] direction).

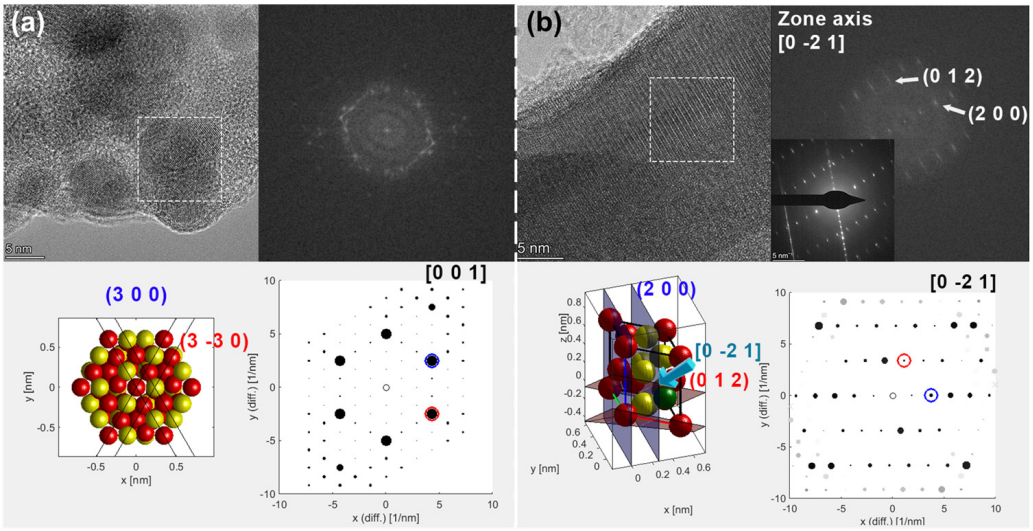

Figure 4. Selected area electron diffraction for (**a**) Cu_3P and (**b**) CuP_2. Experimental diffraction patterns (**top right**) were achieved by Fourier transform of the squared regions, and the calculated patterns (**bottom right**) were generated with CrysTBox [32] with the cif files from Materials Project [33,34].

The survey XPS scans of the as-prepared CuP_2 and Cu_3P are shown in Figure 5a. The C, O, and F peaks can be attributed to the microporous layers (carbon particles and fluoropolymer) of the gas diffusion electrode. The Cu and P contributions are highlighted in blue and red. In the high-resolution scans of P 2p (Figure 5b), the 2p 3/2 spin-orbit peak of CuP_2 is approximately 0.5 eV lower than that observed for Cu_3P, due to the fact that half of the P atoms have a formal valence of zero. The peak at 134.2 eV can be attributed to P-O bonding. The stronger P-O signal observed for Cu_3P is possibly due to the inhomogeneous distribution of P, where a higher P concentration on the surface leads to more surface oxidation, which could also explain the broad peak observed around 30° for the Cu_3P in PXRD. For the Cu 2p (Figure 5c), the binding energies of Cu_3P (952.88 eV for $2p_{1/2}$ and 932.78 eV for $2p_{3/2}$) are almost the same as those observed for CuP_2 (952.98 eV for $2p_{1/2}$ and 932.88 eV for $2p_{3/2}$). The absence of satellite peaks further proves the closed-shell d[10]-configuration of Cu(I).

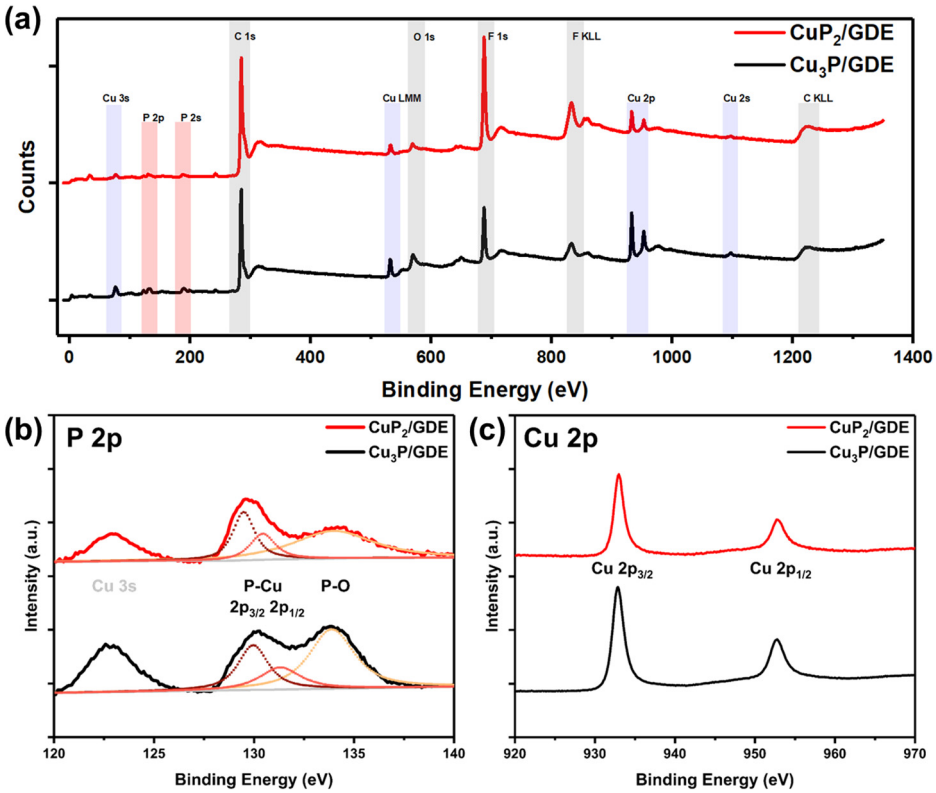

Figure 5. (**a**) Survey scan and high-resolution scan of X-ray photoelectron spectra for (**b**) P 2p and (**c**) Cu 2p; samples were prepared by drop-casting CuP_2 (red) and Cu_3P (black) on gas diffusion electrode.

3.2. Electrochemical Measurements

CuP_2 and Cu_3P were tested as electrocatalysts for the hydrogen evolution reaction (HER) and oxygen evolution reaction (OER) in an alkaline medium. For HER, a three-electrode setup was used, with graphite as the counter electrode and Ag/AgCl as the reference electrode. The catalysts were mixed with carbon black and loaded on glassy carbon for HER. For OER, due to the unstable nature of glassy carbon at high applied potential [35], catalyst inks were drop-cast onto carbon cloth as working electrodes. As shown in Figure 6, both CuP_2 and Cu_3P are better for HER compared to Cu/C. From the LSV, 355 and 460 mV overpotential are required to reach a current density of 1 mA/cm^2 in 0.1 M HCl, and 514 and 388 mV in 0.1 M NaOH, respectively. No iR correction was performed for any of the results presented here. Their Tafel slopes were also calculated and showed similar behavior as Cu. CuP_2 showed better activity than Cu_3P in an acidic environment, while in the alkaline medium, Cu_3P showed a similar slope with Pt and outperformed CuP_2 and Cu. The electrochemical active surface areas of 50 wt% Cu_3P/C and CuP_2/C on glassy carbon were measured in 0.1 M NaOH (Figure S3). The double-layer capacitance for CuP_2/C on glassy carbon was 0.55 mF/cm^2, and 43 mF/cm^2 for Cu_3P/C. Higher double-layer capacitance of CuP_2 compared with Cu_3P demonstrates the advantages of wire-shaped morphology.

For OER, it is known that copper-based material can be oxidized, so the measurements were recorded with cyclic voltammetry until the curves were stable for the acid and alkaline medium. CuP_2 and Cu_3P both showed OER activity for water oxidation (Figure 7). The onset potential of Cu_3P/C and CuP_2/C in 0.1 M HCl is ~1.58 V vs. RHE for both, which is almost the same as 50 wt% RuO_2/C. In 0.1 M NaOH, CuP_2 performed better than Cu_3P, but both are inferior to RuO_2. From electrochemical impedance spectroscopy (EIS), the series resistance (R_s, x-intercepts in Nyquist plot) from the electrode resistance for both Cu_3P and CuP_2 are smaller than that of the bare carbon cloth and remains the same after oxygen evolution reactions. The charge-transfer resistance (R_{CT}) increased dramatically for

both compounds after oxygen evolution reactions due to surface oxidation, but the bulk of the nanocrystals remain the same as indicated by the R_s. The long-term stability and robustness of OER for both materials still need to be improved.

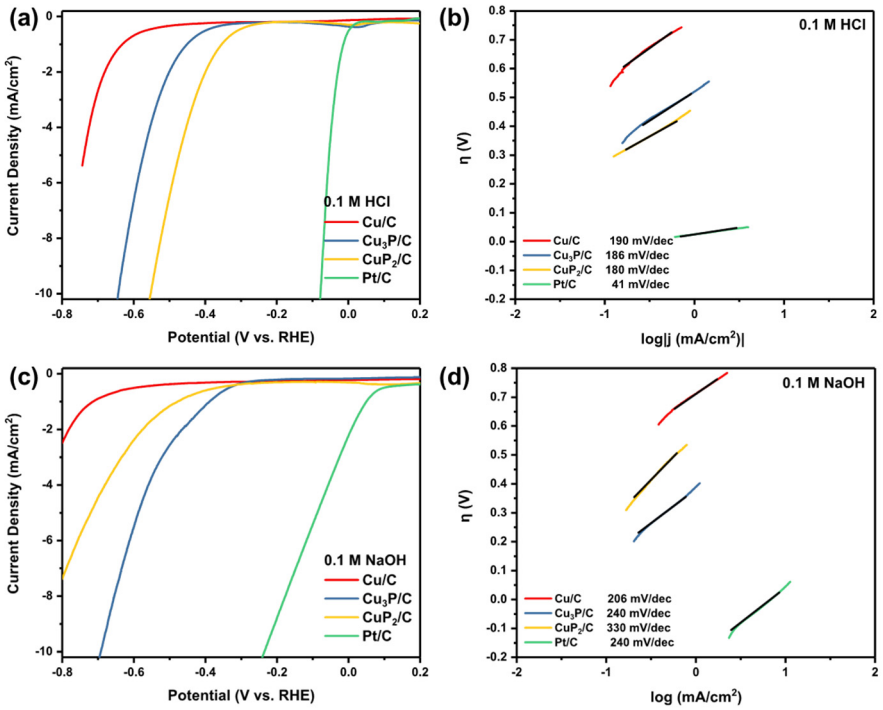

Figure 6. CuP_2 and Cu_3P on glassy carbon for HER and corresponding Tafel analysis in (**a**,**b**) 0.1 M HCl and (**c**,**d**) 0.1 M NaOH.

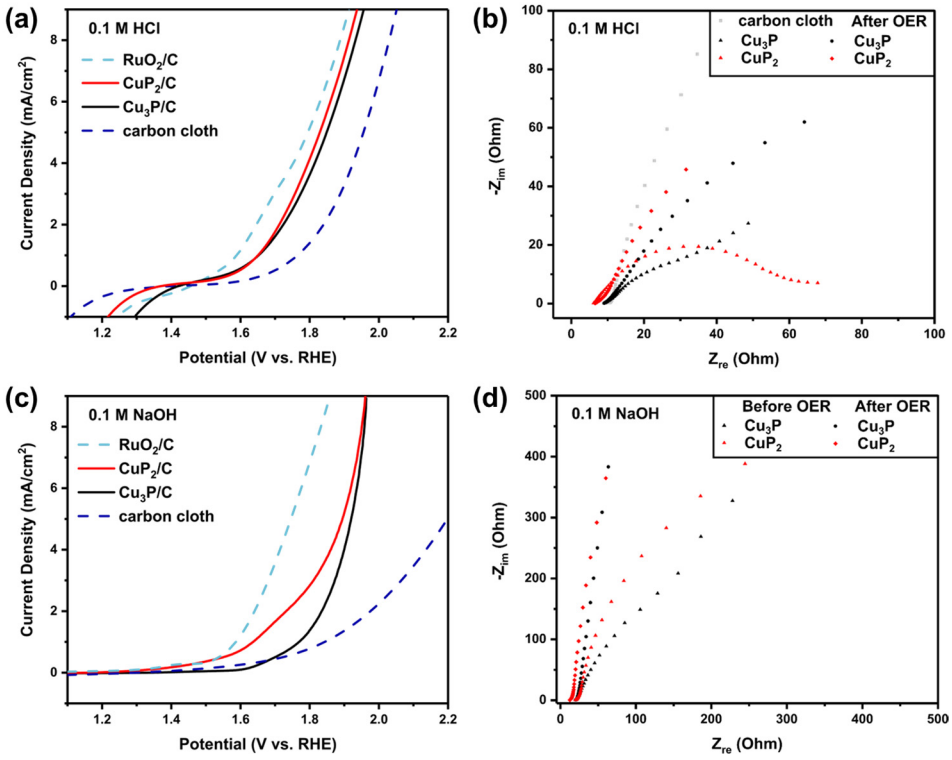

Figure 7. OER and EIS analysis of CuP_2 and Cu_3P on carbon cloth in (**a**,**b**) 0.1 M HCl and (**c**,**d**) 0.1 M NaOH.

For the oxygen reduction reaction, it is important to compare how different P content affects the electrocatalyst activity and durability. As shown in Figure 8, 25 wt% Cu_3P/C outperformed CuP_2/C in onset potential (E_0, 0.72 vs. 0.7 V) and half-wave potential ($E_{1/2}$, 0.60 vs. 0.58 V). The slope from Koutecky–Levich analysis suggests that both Cu_3P and CuP_2 prefer to perform the 2 e^- transfer that generates H_2O_2 instead of the 4 e^- transfer reactions to generate H_2O, and the y-intercept suggests that Cu_3P/C demonstrated a larger kinetic current. Both Cu_3P and CuP_2 showed similar Tafel slopes that were close to that of Ag (90 mV/dec) [36], which also showed 2 e^- transfer behavior. The durability test was performed at 400 rpm for 1000 cycles, and the polarization curves showed a minimal drop for both. To study the catalyst stability in ORR, the catalyst inks were drop-cast onto the gas diffusion electrode and cyclic voltammetry (CV) experiments were performed between 0.4 and 0.8 V (500 mV/s) vs. RHE for 1000 cycles. The XPS spectra for Cu_3P and CuP_2 before and after CV are shown in Figure S4. For Cu_3P, the peaks' positions for P and Cu were the same before and after the 1000 cycles, while CuP_2 had an obvious downshift, especially for the peak corresponding to P-O, which might indicate structural changes after ORR.

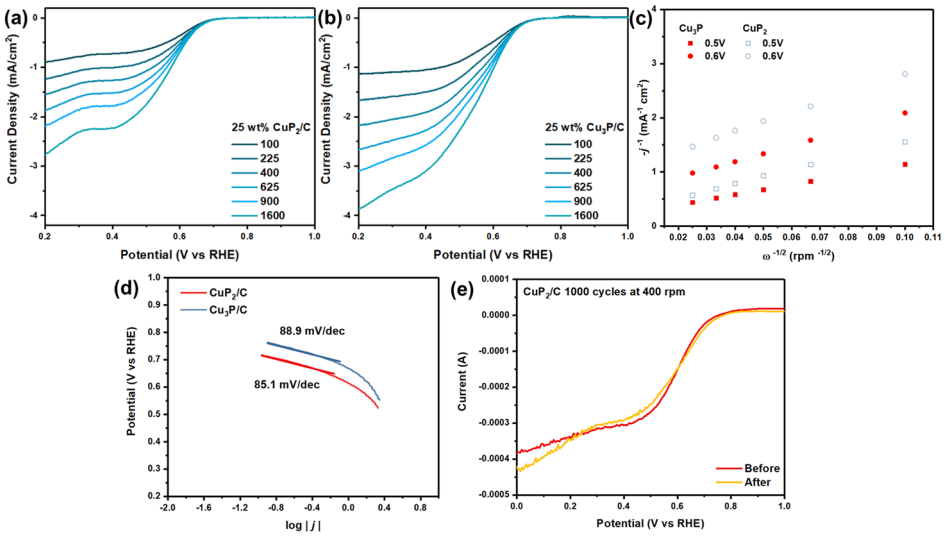

Figure 8. ORR measurements of (**a**) CuP_2/C and (**b**) Cu_3P/C in oxygen-saturated 0.1 M NaOH, and corresponding (**c**) Koutecky–Levich (K-L) analysis. (**d**) Tafel analysis for Cu_3P and CuP_2, and (**e**) durability test for CuP_2/C after 1000 cycles of scans.

4. Conclusions

In summary, highly crystalline CuP_2 was successfully synthesized by the wet chemistry route without additional annealing. The effects of precursors, ligands, solvents and temperature were studied. CuP_2 was obtained with inexpensive red phosphorus as a precursor at a rather low temperature (320 °C). TOPO was found to assist in forming CuP_2 with wire-like morphology, meanwhile, Cu_3P could also be obtained at lower temperatures (250 °C). It was found that, unlike other ligand-assisted colloidal syntheses, the conversion rate is slow for CuP_2 synthesis, and the reaction mechanism is similar to solid-state reactions. Because red phosphorus has less reactivity compared with TOP or TMS_3P, it will allow the generation of more thermodynamically stable products such as CuP_2. This wet-chemical synthesis lowered the temperature required for solid-state synthesis such as vacuum annealing. Also, the reactant can move more freely, allowing TOPO to cap (0 1 2) crystal faces and form nanowires that grow along the [1 0 0] directions.

Furthermore, CuP_2 and Cu_3P have different crystal and electronic structures which affect their electrochemical behavior. CuP_2 works better for HER in acidic conditions and OER in general, while Cu_3P showed better activity than CuP_2 for HER and ORR in an alkaline medium. Both compounds demonstrate similar stability in both alkaline and acidic environments. This synthesis, which controls the stoichiometry and morphology, has the

potential to produce CuP_2 on a large scale for electrochemical and other energy-related studies, such as CO_2 reduction [37] or batteries [38].

Supplementary Materials: The following supporting information can be downloaded at https://www.mdpi.com/article/10.3390/solids5010010/s1, Figure S1. SEM results of morphology differences by increasing TOPO/ODE ratio at the same temperature for CuP_2 synthesis, specifically, 10% for (a), 30% for (b) and 50% for (c). (d) Corresponding diameter distribution histogram of CuP_2 of (c). Figure S2. Typical EDS results for (a) Cu_3P and (b) CuP_2. Figure S3. ECSA comparison of (a,b) 50 wt% CuP_2/C and (b) 50 wt% Cu_3P/C on glassy carbon in 0.1 M NaOH. Figure S4. XPS results for CuP_2 and Cu_3P on gas diffusion electrode after scanned between 0.4 and 0.8 V vs. RHE for 1000 cycles, the results for pristine materials were shown in grey for easier comparison. Figure S5. (a) XRD and (b) EDS results for CuP_2 on carbon cloth (cc) before HER, after HER and after ORR.

Author Contributions: Investigation; data curation and writing—original draft preparation, X.M.; TEM and STEM-EDS, X.H.; writing—review and editing, supervision and funding acquisition, A.L. All authors have read and agreed to the published version of the manuscript.

Funding: X.M. and A.L. would like to acknowledge support from the Sabin Center for the Environment and Sustainability (CEES) and the Center for Functional Materials (CFM) from Wake Forest University. A.L. would like to thank the Fulbright U.S. Scholar Program (13044-WA) for the support.

Data Availability Statement: Data are contained within the article and Supplementary Materials.

Acknowledgments: The authors would like to thank Chaochao Dun from Molecular Foundry for the XPS data measurements.

Conflicts of Interest: The authors declare no conflicts of interest.

References

1. Jiao, Y.; Zheng, Y.; Jaroniec, M.; Qiao, S.Z. Design of Electrocatalysts for Oxygen- and Hydrogen-Involving Energy Conversion Reactions. *Chem. Soc. Rev.* **2015**, *44*, 2060–2086. [CrossRef]
2. Stamenkovic, V.R.; Strmcnik, D.; Lopes, P.P.; Markovic, N.M. Energy and Fuels from Electrochemical Interfaces. *Nat. Mater.* **2017**, *16*, 57–69. [CrossRef]
3. Chen, C.; Kang, Y.; Huo, Z.; Zhu, Z.; Huang, W.; Xin, H.L.; Snyder, J.D.; Li, D.; Herron, J.A.; Mavrikakis, M.; et al. Highly Crystalline Multimetallic Nanoframes with Three-Dimensional Electrocatalytic Surfaces. *Science* **2014**, *343*, 1339–1343. [CrossRef]
4. Liu, J.; Jiao, M.; Lu, L.; Barkholtz, H.M.; Li, Y.; Wang, Y.; Jiang, L.; Wu, Z.; Liu, D.; Zhuang, L.; et al. High Performance Platinum Single Atom Electrocatalyst for Oxygen Reduction Reaction. *Nat. Commun.* **2017**, *8*, 15938. [CrossRef]
5. Zeng, R.; Yang, Y.; Feng, X.; Li, H.; Gibbs, L.M.; DiSalvo, F.J.; Abruña, H.D. Nonprecious Transition Metal Nitrides as Efficient Oxygen Reduction Electrocatalysts for Alkaline Fuel Cells. *Sci. Adv.* **2022**, *8*, eabj1584. [CrossRef]
6. Ren, X.; Wang, H.; Chen, J.; Xu, W.; He, Q.; Wang, H.; Zhan, F.; Chen, S.; Chen, L. Emerging 2D Copper-Based Materials for Energy Storage and Conversion: A Review and Perspective. *Small* **2023**, *19*, 2204121. [CrossRef]
7. Jiang, P.; Liu, Q.; Liang, Y.; Tian, J.; Asiri, A.M.; Sun, X. A Cost-Effective 3D Hydrogen Evolution Cathode with High Catalytic Activity: FeP Nanowire Array as the Active Phase. *Angew. Chem. Int. Ed.* **2014**, *53*, 12855–12859. [CrossRef]
8. Lu, X.F.; Yu, L.; Lou, X.W. Highly Crystalline Ni-Doped FeP/Carbon Hollow Nanorods as All-pH Efficient and Durable Hydrogen Evolving Electrocatalysts. *Sci. Adv.* **2019**, *5*, eaav6009. [CrossRef] [PubMed]
9. Gong, M.; Li, Y.; Wang, H.; Liang, Y.; Wu, J.Z.; Zhou, J.; Wang, J.; Regier, T.; Wei, F.; Dai, H. An Advanced Ni–Fe Layered Double Hydroxide Electrocatalyst for Water Oxidation. *J. Am. Chem. Soc.* **2013**, *135*, 8452–8455. [CrossRef] [PubMed]
10. Tanaka, Y.; Onoda, A.; Okuoka, S.; Kitano, T.; Matsumoto, K.; Sakata, T.; Yasuda, H.; Hayashi, T. Nonprecious-Metal Fe/N/C Catalysts Prepared from π-Expanded Fe Salen Precursors toward an Efficient Oxygen Reduction Reaction. *ChemCatChem* **2018**, *10*, 743–750. [CrossRef]
11. Hu, X.; Chen, S.; Chen, L.; Tian, Y.; Yao, S.; Lu, Z.; Zhang, X.; Zhou, Z. What Is the Real Origin of the Activity of Fe–N–C Electrocatalysts in the O_2 Reduction Reaction? Critical Roles of Coordinating Pyrrolic N and Axially Adsorbing Species. *J. Am. Chem. Soc.* **2022**, *144*, 18144–18152. [CrossRef]
12. Zhou, Z.; Li, X.; Li, Q.; Zhao, Y.; Pang, H. Copper-Based Materials as Highly Active Electrocatalysts for the Oxygen Evolution Reaction. *Mater. Today Chem.* **2019**, *11*, 169–196. [CrossRef]
13. Cracknell, J.A.; Vincent, K.A.; Armstrong, F.A. Enzymes as Working or Inspirational Electrocatalysts for Fuel Cells and Electrolysis. *Chem. Rev.* **2008**, *108*, 2439–2461. [CrossRef]
14. Thorseth, M.A.; Tornow, C.E.; Tse, E.C.M.; Gewirth, A.A. Cu Complexes That Catalyze the Oxygen Reduction Reaction. *Coord. Chem. Rev.* **2013**, *257*, 130–139. [CrossRef]

15. Parra-Puerto, A.; Ng, K.L.; Fahy, K.; Goode, A.E.; Ryan, M.P.; Kucernak, A. Supported Transition Metal Phosphides: Activity Survey for HER, ORR, OER, and Corrosion Resistance in Acid and Alkaline Electrolytes. *ACS Catal.* **2019**, *9*, 11515–11529. [CrossRef]
16. Pu, Z.; Liu, T.; Amiinu, I.S.; Cheng, R.; Wang, P.; Zhang, C.; Ji, P.; Hu, W.; Liu, J.; Mu, S. Transition-Metal Phosphides: Activity Origin, Energy-Related Electrocatalysis Applications, and Synthetic Strategies. *Adv. Funct. Mater.* **2020**, *30*, 2004009. [CrossRef]
17. Harper, A.F.; Evans, M.L.; Morris, A.J. Computational Investigation of Copper Phosphides as Conversion Anodes for Lithium-Ion Batteries. *Chem. Mater.* **2020**, *32*, 6629–6639. [CrossRef] [PubMed]
18. Zhao, C.; Chen, H.; Liu, H.; Yin, L.; Zhang, Q.; Yu, S.; Liu, P.; Zhong, G.; Lu, C.-Z.; Yang, Y. Quantifying the Reaction Mechanisms of a High-Capacity CuP2/C Composite Anode for Potassium Ion Batteries. *J. Mater. Chem. A* **2021**, *9*, 6274–6283. [CrossRef]
19. Crovetto, A.; Kojda, D.; Yi, F.; Heinselman, K.N.; LaVan, D.A.; Habicht, K.; Unold, T.; Zakutayev, A. Crystallize It before It Diffuses: Kinetic Stabilization of Thin-Film Phosphorus-Rich Semiconductor CuP2. *J. Am. Chem. Soc.* **2022**, *144*, 13334–13343. [CrossRef] [PubMed]
20. Rachkov, A.G.; Schimpf, A.M. Colloidal Synthesis of Tunable Copper Phosphide Nanocrystals. *Chem. Mater.* **2021**, *33*, 1394–1406. [CrossRef]
21. Kim, S.-O.; Manthiram, A. The Facile Synthesis and Enhanced Sodium-Storage Performance of a Chemically Bonded CuP2/C Hybrid Anode. *Chem. Commun.* **2016**, *52*, 4337–4340. [CrossRef]
22. Muruganantham, R.; Chiang, P.-C.; Liu, W.-R. Copper-Diphosphide Composites: A Key Factor Evaluation and Capacity Enhancement Route for High-Energy Lithium-Ion Storage. *ACS Appl. Energy Mater.* **2018**, *1*, 3674–3683. [CrossRef]
23. Li, G.-A.; Wang, C.-Y.; Chang, W.-C.; Tuan, H.-Y. Phosphorus-Rich Copper Phosphide Nanowires for Field-Effect Transistors and Lithium-Ion Batteries. *ACS Nano* **2016**, *10*, 8632–8644. [CrossRef] [PubMed]
24. Barry, B.M. Synthesis of Transition-Metal Polyphosphides. Ph.D. Thesis, University of Iowa, Iowa City, IA, USA, 2010. [CrossRef]
25. Barry, B.M.; Gillan, E.G. A General and Flexible Synthesis of Transition-Metal Polyphosphides via PCl3 Elimination. *Chem. Mater.* **2009**, *21*, 4454–4461. [CrossRef]
26. Coleman, N., Jr.; Lovander, M.D.; Leddy, J.; Gillan, E.G. Phosphorus-Rich Metal Phosphides: Direct and Tin Flux-Assisted Synthesis and Evaluation as Hydrogen Evolution Electrocatalysts. *Inorg. Chem.* **2019**, *58*, 5013–5024. [CrossRef] [PubMed]
27. Wolff, A.; Doert, T.; Hunger, J.; Kaiser, M.; Pallmann, J.; Reinhold, R.; Yogendra, S.; Giebeler, L.; Sichelschmidt, J.; Schnelle, W.; et al. Low-Temperature Tailoring of Copper-Deficient Cu3–xP—Electric Properties, Phase Transitions, and Performance in Lithium-Ion Batteries. *Chem. Mater.* **2018**, *30*, 7111–7123. [CrossRef]
28. Downes, C.A.; Libretto, N.J.; Harman-Ware, A.E.; Happs, R.M.; Ruddy, D.A.; Baddour, F.G.; Ferrell III, J.R.; Habas, S.E.; Schaidle, J.A. Electrocatalytic CO_2 Reduction over Cu_3P Nanoparticles Generated via a Molecular Precursor Route. *ACS Appl. Energy Mater.* **2020**, *3*, 10435–10446. [CrossRef]
29. Barry, B.M.; Gillan, E.G. Low-Temperature Solvothermal Synthesis of Phosphorus-Rich Transition-Metal Phosphides. *Chem. Mater.* **2008**, *20*, 2618–2620. [CrossRef]
30. Penn, R.L.; Banfield, J.F. Morphology Development and Crystal Growth in Nanocrystalline Aggregates under Hydrothermal Conditions: Insights from Titania. *Geochim. Cosmochim. Acta* **1999**, *63*, 1549–1557. [CrossRef]
31. Dolgin, B.P. Kinetics of the Formation of an Amorphous Layer During a Solid State Reaction. Ph.D. Thesis, California Institute of Technology, Pasadena, CA, USA, 1985. [CrossRef]
32. Klinger, M.; Jäger, A. Crystallographic Tool Box (CrysTBox): Automated Tools for Transmission Electron Microscopists and Crystallographers. *J. Appl. Crystallogr.* **2015**, *48*, 2012–2018. [CrossRef]
33. Mp-14012: Cu3P (Trigonal, P-3c1, 165). Available online: https://next-gen.materialsproject.org/materials/mp-14012?chemsys=Cu-P (accessed on 4 September 2023).
34. mp-927: CuP2 (Monoclinic, P2_1/c, 14). Materials Project. Available online: https://next-gen.materialsproject.org/materials/mp-927?_sort_fields=energy_above_hull&chemsys=Cu-P (accessed on 4 September 2023).
35. Yi, Y.; Weinberg, G.; Prenzel, M.; Greiner, M.; Heumann, S.; Becker, S.; Schlögl, R. Electrochemical Corrosion of a Glassy Carbon Electrode. *Catal. Today* **2017**, *295*, 32–40. [CrossRef]
36. Higgins, D.; Wette, M.; Gibbons, B.M.; Siahrostami, S.; Hahn, C.; Escudero-Escribano, M.; García-Melchor, M.; Ulissi, Z.; Davis, R.C.; Mehta, A.; et al. Copper Silver Thin Films with Metastable Miscibility for Oxygen Reduction Electrocatalysis in Alkaline Electrolytes. *ACS Appl. Energy Mater.* **2018**, *1*, 1990–1999. [CrossRef]
37. Choi, M.; Bong, S.; Kim, J.W.; Lee, J. Formation of 1-Butanol from CO_2 without *CO Dimerization on a Phosphorus-Rich Copper Cathode. *ACS Energy Lett.* **2021**, *6*, 2090–2095. [CrossRef]
38. Kim, S.-O.; Manthiram, A. Phosphorus-Rich CuP_2 Embedded in Carbon Matrix as a High-Performance Anode for Lithium-Ion Batteries. *ACS Appl. Mater. Interfaces* **2017**, *9*, 16221–16227. [CrossRef] [PubMed]